Rare Metal Materials and Engineering
Volume 54, Issue 8, August 2025
Available online at www.rmme.ac.cn

Science Press

Cite this article as: Xu He, Liang Jingjing, Li Jinguo. Microstructure and Mechanical Properties of New Nickel-Based Superalloys Fabricated by Selective Laser Melting at Low Energy Density[J]. Rare Metal Materials and Engineering, 2025, 54(08): 1926-1933. DOI: https://doi.org/10.12442/j.issn.1002-185X.20240421.

ARTICLE

Microstructure and Mechanical Properties of New Nickel-Based Superalloys Fabricated by Selective Laser Melting at Low Energy Density

Xu He[1,2], Liang Jingjing[1,2], Li Jinguo[1,2]

[1] School of Materials Science and Engineering, University of Science and Technology of China, Shenyang 110016, China; [2] Shi-changxu Innovation Center for Advanced Materials, Institute of Metal Research, Chinese Academy of Sciences, Shenyang 110016, China

Abstract: ZGH401 alloy was prepared under varying laser power levels and scanning speeds by the orthogonal test method using selective laser melting (SLM). The effect of different energy densities on microstructure and mechanical properties of the formed alloy was investigated. The microstructure of ZGH401 was analyzed by scanning electron microscope, electron back-scattered diffraction, and electron probe microanalysis. The results show that the defects of the as-built ZGH401 are gradually reduced, the relative density is correspondingly enhanced with increasing the energy density, and the ultimate density can reach 99.6%. An increase in laser power leads to a corresponding rise in hardness of ZGH401, while a faster scanning speed reduces the residual stress in as-built ZGH401 samples. In addition, better tensile properties are achieved at room temperature due to more grain boundaries perpendicular to the build direction than parallel to the build direction. The precipitated phases are identified as carbides and Laves phases via chemical composition analysis, with fewer carbides observed at the molten pool boundaries than within the molten pools.

Key words: selective laser melting; low energy density; ZGH401

1 Introduction

Additive manufacturing (AM), also known as 3D printing, can create intricately shaped structures hard to or impossible to construct usually, marking it a novel technical approach for producing superalloy components. AM can overcome certain drawbacks of conventional methods, and there remain fundamental issues to address prior to its mass application in industries. A significant concern is the residual stress and micro-cracks induced by thermal gradients during the processing stage. Several Ni-based superalloys are known to be susceptible to micro-cracking, thereby restricting their application in the manufacturing of aerospace parts[1–2]. Selective laser melting (SLM), a prominent AM technique, enables the rapid, cost-efficient production of high-precision components with intricate geometries. SLM has attracted increasing attention as an advanced biomedical device manufacturing method[3–4].

Shahwaz et al[5] provided a comprehensive overview of the effect of SLM on the microstructure evolution as well as properties of additively manufactured IN625 and IN718 alloys. The main reason for the excellent properties of nickel-based superalloys is two reinforcing precipitation phases, γ' (Ni_3Al) and γ'' (Ni_3Nb)[6–8]. At higher service temperatures, γ' has a stronger thermal stability than the γ'' phase. The explanation given so far is that the effect of γ' phase on the mechanical properties of alloys at high temperatures is superior to that of γ'' phase, possibly due to the transformation of γ'' phase into δ phase at high temperatures, which degrades the mechanical properties of alloys[9–11]. Based on this, Al, Ti, and Nb serve to promote the formation of strengthening phases, while W and Mo strengthen the matrix via solid solution hardening. Rare earth elements inhibit coarsening of the γ' phase. C and B are added to form carbides at grain

Received date: July 12, 2024
Foundation item: National Defense Science and Technology Project Management Center (2021-JCJQ-JJ-0092)
Corresponding author: Li Jinguo, Ph. D., Professor, Institute of Metal Research, Chinese Academy of Sciences, Shenyang 110016, P. R. China, Tel: 0086-24-83978872, E-mail: jgli@imr.ac.cn; Liang Jingjing, Ph. D., Professor, Institute of Metal Research, Chinese Academy of Sciences, Shenyang 110016, P. R. China, Tel: 0086-24-23971787, E-mail: jjliang@imr.ac.cn

boundaries, thereby preventing grain boundary slippage and enhancing creep resistance[12–14].

The layer-by-layer deposition, melting, and solidification processes in the AM process cause significant microstructure evolution. Fish-scale-like semicircular rings can be observed in different classes of additively fabricated nickel-based superalloys[15–17]. These rings mainly indicate the movement of the laser tip and subsequent formation of the molten pool. The opening spacing, layer thickness, as well as columnar versus equiaxed crystals, can be seen in the molten pool morphology[18–19]. The microstructure of a typical additively fabricated nickel-based superalloy consists of a γ matrix, reinforcing phases, *M*C-type carbides precipitated at grain boundaries, and Laves phases consisting of Ti and Nb[20–22]. Studies indicate that the formation of the Laves phase is primarily attributed to segregation of Nb during solidification processes. To enhance material properties and to relieve residual thermal stresses induced during AM, solution treatment followed by annealing were conducted on the alloy. The heat treatment promotes the transformation of γ'' at grain boundaries into brittle needle-like δ-phase with Laves phase. Additionally, primary *M*C carbides decompose into $M_{23}C_6$ and M_6C carbides. The Laves phase, a hard and brittle intermetallic, is susceptible to cracking under mechanical stress. The δ-phase will reduce the γ-phase content, whereas the Laves phase will decrease the δ-phase content, which is composed of Ti and Nb. Thus the δ phase reduces the γ'' content. The low-temperature microstructural uniformity and mechanical properties of superalloys can be improved by δ-phase solid solution treatment.

The ZGH401 is a high-performance nickel-based superalloy specially designed for AM by the Institute of Metals, Chinese Academy of Sciences. Wu et al[23] studied the fabrication of ZGH401 via laser metal deposition. The main phase constituents of the ZGH401 alloy are γ and γ' phases, along with minor fractions of Laves phase and *M*C carbides. The primary dendrite arm spacing (PDAS) for the deposited alloy measures approximately 15–50 μm, with an average γ' phase diameter ranging from 100 nm to 150 nm; in contrast, the as-cast alloy spans 300 – 500 μm and 200 – 350 nm. Decreased PDAS enhances the microstructural uniformity in alloys, thereby suppressing the formation of detrimental phases. This refinement significantly amplifies the strengthening effect of alloy components, ultimately improving mechanical properties. Within a wide processing window, the as-deposited alloy maintains structural integrity and exhibits no cracking during fabrication. This alloy features a cellular dendrite that expands along the crystallographic direction [001], aligning with the deposition direction. The elements Al, Cr, Co, Nb, and Ti possess higher concentrations in the dendrite core region and the interdendritic region[23–24].

However, these studies are focused primarily on additive manufactured ZGH401. The current shortcomings are the lack of comprehensive, in-depth, systematic research on the microstructure and properties of the SLM fabricated ZGH401. To facilitate the development of the alloy from research to industrial application and to design advanced alloys, this research focused on the microstructure, morphology, density, hardness, and residual stresses of ZGH401 fabricated via SLM under low energy density conditions.

2 Experiment

2.1 Powder properties

The chemical composition of ZGH401 is listed in Table 1. The powder was produced using vacuum-induced gas atomization in the Institute of Metal Research. ZGH401 powders consist of the following chemical compositions: 20wt% Cr+Co, 9.2wt% Hf+Mo+Nb, 4.5wt% Al+Ti, 0.46wt% C+Si, and the balance Ni.

According to the composition in Table 1, alloy was melted in a vacuum induction furnace to cast an ingot, which was then processed into gas-atomized powder via inert gas atomization. The powder was sieved to isolate particles within the 270-800 mesh range (18–53 μm in diameter).

Inspect F50 scanning electron microscope (SEM) and the Bettersize 2600 laser particle size distributor were used to assess the shape and size of the powder. As shown in Fig. 1, most of the particles are spherical in shape, while only a few powders have satellite attachments. The average diameter of powders is 34.50 μm. In addition, D_{10}=20.87 μm, D_{50}=35.79 μm, and D_{90}=51.15 μm.

2.2 Sample preparation

Prior to SLM, the ZGH401 powder was dried at 200 °C for 3 h to eliminate moisture. A Concept Laser M2 machine was used to conduct the SLM experiments. The SLM process was conducted under a high-purity Ar atmosphere (with the oxygen content in the forming chamber below 1000 μL/L), using a 316L stainless steel plate as the base material. Throughout the SLM procedure, the plate underwent preheating to 105 °C. The dimensions of the sample measured

Table 1 Element composition of alloys (wt%)

Al+Ti	Co+Cr	Hf+Mo+Nb	Si+C	Ni
4.5	20	9.2	0.46	Bal.

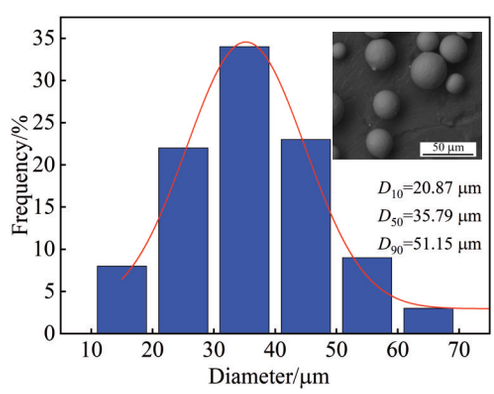

Fig.1 Particle size distribution of gas-atomized ZGH401 powders and SEM image

15 mm×15 mm×20 mm, and its morphology is depicted in Fig. 2a. In addition, in order to test the mechanical properties in different directions, two types of samples with dimensions of 20 mm×20 mm×55 mm were prepared, as shown in Fig. 2b. The parameters for the process are listed in Table 2. The laser power (P) was 200, 220, 240, 260, 280, and 300 W. The thickness (d) of the layer measured 50 μm, with a hatch spacing (h) of 120 μm. There was no angular rotation in the scanning approach between the neighboring layers (Fig. 2c), and the speed of scanning (v) was 750, 800, 850, 900, 950, and 1000 mm/s. From the above process parameters, energy densities (E) in this SLM process can be calculated by Eq. (1). The range of energy density was between 33.33–66.67 J/mm^3.

$$E=P/vhd \quad (1)$$

After SLM, the sample was cut from the substrate. Composition analysis via X-ray fluorescence spectroscope showed that the as-fabricated alloy closely matched the initial powder composition.

2.3 Microstructure observation

The samples were produced in cubic forms measuring 15 mm×15 mm×20 mm. For cross-sectional analysis, the samples were sliced along the axis that aligns with the construction direction. Polishing of the sectioned area was conducted by 180#, 240#, 400#, 800#, 1000#, and 2000# abrasive sandpapers. The samples were corroded using $CuCl_2$, HCl, and C_2H_5OH. ZEISS Sigma-300 SEM was used to observe the microstructure. Additional elemental analysis was conducted using a JXA-iHP20 electron probe microanalyzer (EPMA).

2.4 Property measurement

The Vickers hardness was tested at a load of 4.9 N at 23 °C according to GB/T 4340.1-2009. The mean value was determined by assessing three specific points on the cross-sectional area. The samples of 20 mm×20 mm×55 mm were cut from the substrate and processed into M6ϕ3 samples. The tensile tests were conducted according to Plan B in GB/T 228.1-2021. Likewise, three sets of parallel samples were tested. In addition, according to GB/T 31218-2014, the center point of the upper surface of the sample was tested by KJS-3 (309001) residual stress tester.

3 Results

3.1 Porosity

The energy density corresponding to each process was calculated using Eq. (1). Samples were then cut along the build direction, and cross-sectional defects were observed by optical microscope (OM), as shown in Fig. 3. The black dots in the figure denote porosity. Cross-sectional images of 36 samples were systematically arranged, as shown in Fig. 3a, which clearly shows that porosity increases with increasing the scanning rate, while increasing laser power reduces porosity. This indicates that energy density is the primary factor governing porosity: the higher the energy density, the lower the porosity. At low laser power levels, insufficient energy input results in inadequate molten pool alignment between the molten pool and solidification front, leading to incomplete fusion of alloy powder. This manifests as spherification and porosity. As the laser power intensifies, the powder within the molten pool completely dissolves, which makes the density increase. When the scanning rate is excessively high, insufficient energy input leads to incomplete fusion of powder particles, resulting in the formation of more pores.

Analyzed by JMatPro software, the theoretical density of ZGH401 alloy is 8.24 g/cm^3. The density assessments were conducted in accordance with the renowned Archimedes ' technique, ensuring a minimum of three repetitions per SLM sample. The result is shown in Fig. 3. It is clear that the difference in density is due to different porosities. To validate the correlation between density and porosity of SLM-formed components, Image J software was used for quantitative analysis of polished cross-sections for selected samples. The fractional area occupied by internal porosities was quantified, and the results are presented in Fig. 3b. When the laser power is 200 W and the scanning rate is 1000 mm/s, the energy density of the alloy is only 33.33 J/mm^3 in Fig. 3c, the porosity reaches 5.8%, and the density is only 7.91 g/cm^3. When the laser power is 300 W and the scanning rate is 750 mm/s, the energy density of the alloy is 66.66 J/mm^3 in Fig. 3d. With increasing energy density from 33.33 to 66.67 J/mm^3, porosity

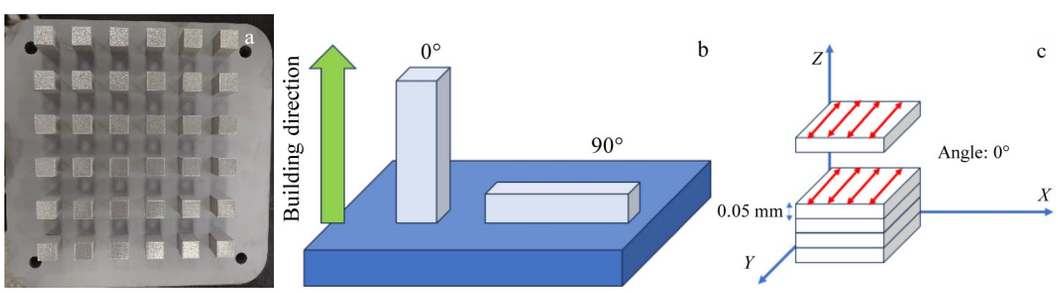

Fig. 2 Smaller-sized samples (a) and two kinds of larger-sized samples in different directions (b); scanning strategy (c)

exhibits a steep decline from >5.2% to <0.08%, accompanied by a density increase from 7.91 to 8.21 g/cm^3. Defining 0.1% porosity as the quality control threshold, the corresponding energy density of about 46 J/mm^3 marks the inflection point

Table 2 Process parameters for the production of samples

P/W	v/mm·s^{-1}	h/mm	d/mm	E/J·mm^{-3}
200–300	750–1000	0.12	0.05	33.33–66.67

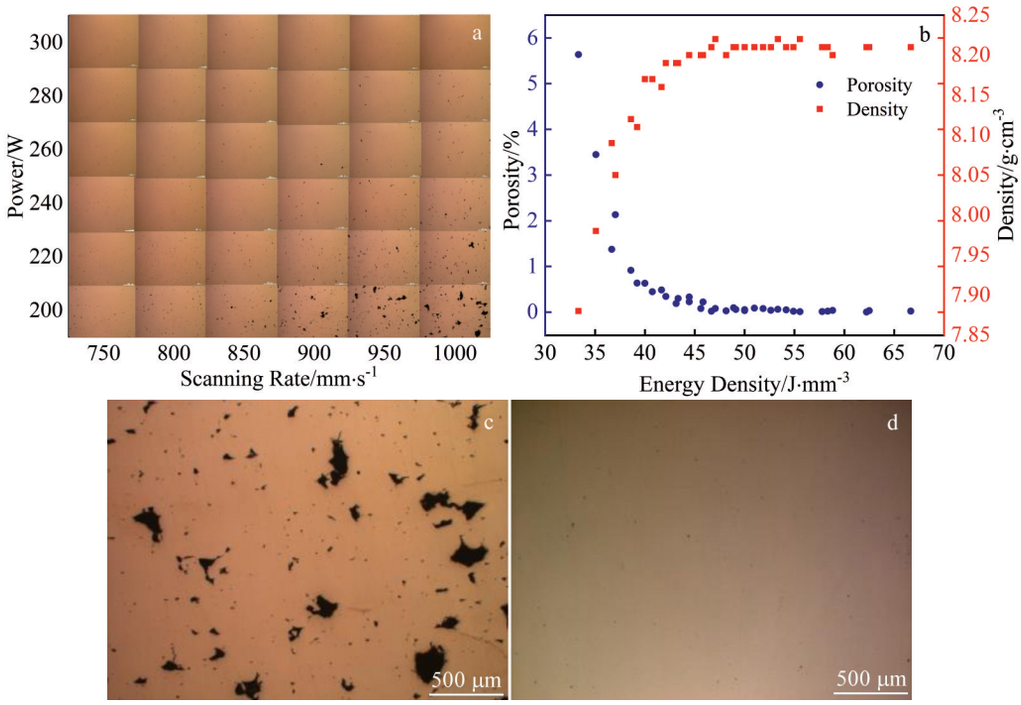

Fig.3 OM morphologies under different parameters (a); correlation between density and internal porosity of SLM-formed samples (b); morphologies at 200 W, 1000 mm/s (c) and at 300 W, 750 mm/s (d)

for transitioning from porous to fully densified microstructures. To achieve the alloy with qualified density, the energy density must be maintained above 46 J/mm³ during processing.

3.2 Hardness and residual stress

Fig.4 shows the relationship between hardness, laser power, and scanning rate during the optimized SLM process of ZGH401. At a laser power of 300 W, increasing the scanning rate from 800 to 1000 mm/s results in a decrease in hardness from 362 to 349 HV. In the same pattern, the hardness decreases with increasing the scanning rate when the laser power is 220 and 260 W. Hardness increases with increasing the laser power at a constant scanning rate.

Hardness characterizes a material's resistance to localized plastic deformation. In alloys with high porosity, the presence of voids reduces load-bearing capacity and induces stress concentrations, leading to premature deformation and lower hardness. As energy density increases, improved powder fusion reduces the pores to obtain a denser microstructure, thereby enhancing hardness.

Fig. 5 illustrates the outcomes of residual stress under varying energy density scenarios. Under conditions of minimal laser power and maximal scanning speed, residual stress occasionally reaches 411.5 MPa. Conversely, at maximum laser power and minimal scanning speed, the average residual stress decreases to 359.5 MPa.

The longer duration of laser exposure to a specific region can lead to a rise in its temperature, which in turn affects the material's laser absorption rate. As scanning velocity decreases, laser exposure duration increases, leading to higher peak temperatures and enhanced absorption rate to laser energy. Consequently, there is a swift rise in thermal energy,

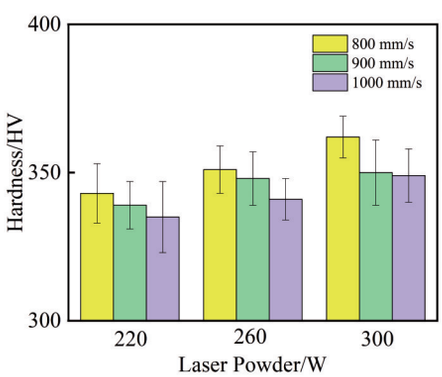

Fig.4 Variation of hardness of ZGH401 with laser power

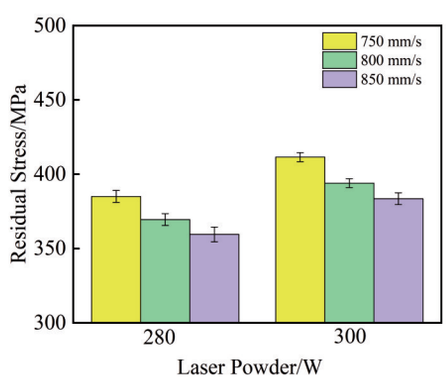

Fig.5 Comparison of residual stress under varying energy densities

hastening the thermal residual stress as the cooling process is intensified. Among the process parameters, scanning speed is the most influential variable: a reduction in scanning speed leads to heightened laser exposure and increased residual stress[25–26].

3.3 Microstructure

The microstructures of SLM-formed samples with different bulk energy densities are similar to that of samples with a bulk energy density of 66.67 J/mm^3. For example, from Fig. 6a, SLM-formed ZGH401 alloy exhibits a fish scale-like morphology in the longitudinal section. These fish scales should be formed by the solidification of the molten pool, and the same deposition layer scanning line between the lap is good, with no porosity.

It can be seen from Fig. 6b–6c that the columnar crystal of ZGH401 alloy grows along the crystallographic direction [001], aligning with the deposition direction. During the production of ZGH401 samples with SLM, the energy input and cooling process result in the formation of columnar grains, which is accountable for the anisotropic mechanical characteristics of the as-built samples. Various process parameters collectively control the heat transfer process in AM and influence the resulting anisotropic mechanical properties. The semi-elliptical morphologies of the molten pools are clearly visible, and measured depths and widths of molten pool are 80 and 140 μm, respectively. It is observed that certain grains, measuring 30 – 80 μm in width, traverse several molten pools in the constructed direction via epitaxial growth. An unbroken line measuring 0.1–0.2 μm in thickness was positioned at the edges of the grains, which are expected to contain carbide precipitates. Comprising fine columnar and cellular subgrains, these sizable grains represent common solidification microstructures found in laser powder bed fusion-nickel-based superalloys. The columnar subgrain with 0.5 – 1.5 μm in width and 6 – 16 μm in length is lined with continuous thin layers or intermittent chains of particles. The majority of cellular subgrains, averaging around 1.4 μm in size, are found near the boundaries of the molten pool, with a few carbide granules scattered along these cellular subgrain boundaries.

Fig. 7 shows typical microstructures of the as-built ZGH401 sample along the build direction. The heavily enriched elements are C and Nb in carbide precipitates. The rest elements (Hf, Si, and Ti) are only slightly enriched. It is known that SLM-formed nickel-based superalloys consist of a γ matrix, γ' precipitates, carbides precipitated along grain boundaries, and a Laves phase rich in Ti and Nb. Studies have shown that the formation of the Laves phase is caused by the partial precipitation of Nb. Based on this, it is hypothesized that the precipitated phase is composed of *M*C carbides that form subgrains aligned with grains in the build direction, as well as the Laves phase.

3.4 Mechanical properties

According to Fig. 2, samples of 20 mm×20 mm×55 mm were cut from the substrate and processed into M6ϕ3 specifications. Two types of samples with different orientations were tested at the same time, which were parallel to the building direction and perpendicular to the building direction. A total of ten samples were tested, and their tensile properties at room temperature are shown in Table 3. The maximum tensile strength perpendicular to the building direction is 1160 MPa. Additionally, the mechanical properties of samples in different build orientations are compared under identical process conditions, revealing significant discrepancies in properties between the two orientations. The average values are 1147.6 (90°) and 1122.5 MPa (0°), separately. The maximum and minimum gaps are 41 and 11 MPa, respectively. Their average value is 25.10 MPa.

Samples oriented parallel to the build direction are taller than that perpendicular to the build direction, requiring more

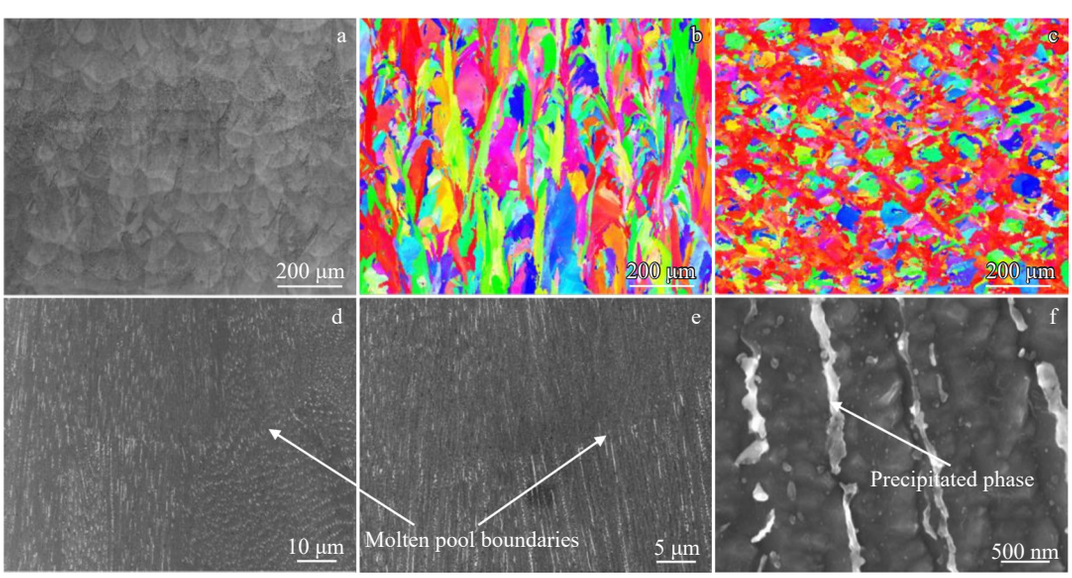

Fig.6 SEM image (a) and EBSD maps in the longitudinal section (perpendicular to the building direction) (b) and cross section (c); SEM images of the molten pool (d–f)

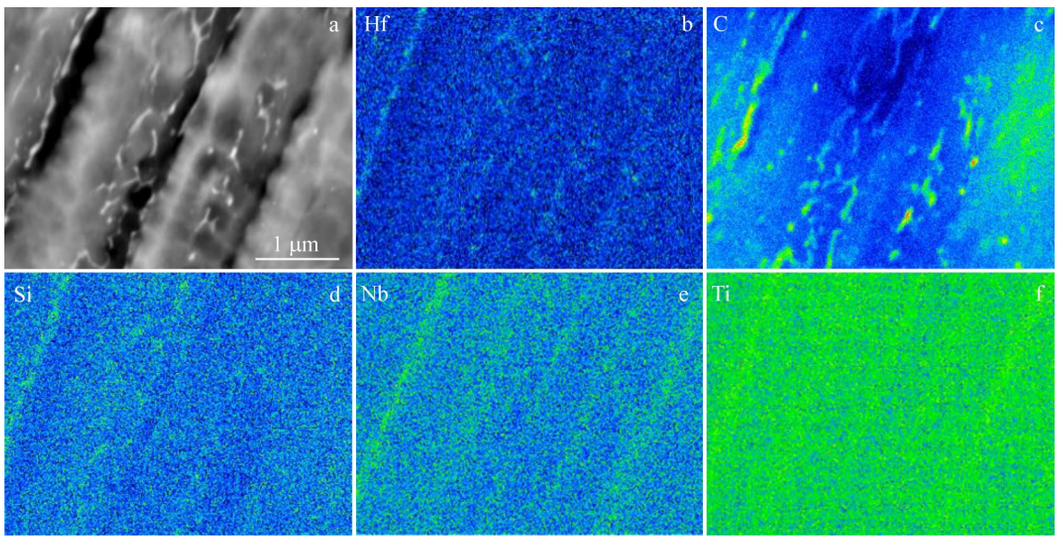

Fig.7 Microstructure (a) and elemental mappings (b–f) of as-built ZGH401 characterized by EPMA

Table 3 Tensile strength of ten as-built samples parallel (0°) and perpendicular (90°) to the building direction at room temperature (MPa)

Sample	90°	0°	Gap/MPa
1	1150	1120	30
2	1146	1118	28
3	1148	1121	27
4	1159	1127	32
5	1138	1120	18
6	1136	1125	11
7	1157	1131	26
8	1160	1119	41
9	1139	1119	20
10	1143	1125	18

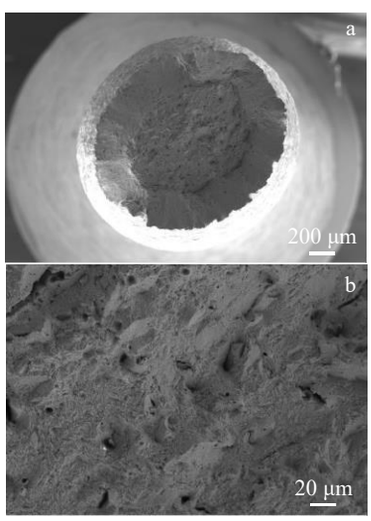

Fig.8 Tension fracture morphologies of as-built ZGH401 samples at 25 ℃

layers and longer processing durations, and thus resulting in a higher probability of defect formation. This is contributed to anisotropy and tensile properties of samples parallel to the build direction. A more important reason is that the grain boundaries parallel to the build direction are larger than that perpendicular to the build direction, which are thought to contribute to the inferior mechanical anisotropy and tensile properties of samples parallel to the build direction[27–28]. Therefore, during the SLM fabrication of alloy components, careful consideration for the build direction is critical to optimize mechanical properties.

Fig. 8 shows the tension test results of as-built ZGH401 alloy at 25 ℃. The fracture surface exhibits distinct fiber and shear lip zones, both characterized by dimpled rupture. Notably, the dimple depths within these zones are comparable.

4 Discussion

The SLM process involves a multifaceted process of transferring heat. The intense energy emitted by the laser is conveyed to the powder layer, leading to the melting of the metal powder. During the AM process, localized areas of the sample are rapidly heated and cooled by hot endpoints, which tend to induce temperature gradients, and the positional differences in this case lead to inconsistent expansion and contraction, which in turn generate large amounts of thermal stress within the sample. Thermal stress is an important source of residual stress in the AM process. During the heating stage, the thermal expansion of the newly deposited layer is restricted by the previously solidified layer, resulting in compressive strains; during the cooling stage, the contraction of the upper layer generates tensile residual stresses that can be balanced by compressive stresses in the surrounding region. Furthermore, as the metal sample is produced sequentially, the solidification shrinkage of molten layers overlays, creating tensile residual stresses on the

uppermost layer ' s surface. When this phenomenon occurs across various layers, the residual stress on the surface of the sample is usually tensile stress, which is also consistent with the results measured in this study. For alloys in the as-deposited state, either increasing the laser power or decreasing the scanning rate will increase the temperature gradient, resulting in residual stresses, so it can be argued that when determining one of these parameters, an increase in energy density will indeed result in an increase in residual stresses.

In general, the main reasons for differences in hardness should be analyzed in terms of cracks, holes, grains, and the residual stress state of the alloy. The state of residual stress does affect the hardness, but for the as-built sample, the grains under different energy densities will not change much, and the residual stress is all tensile stress with different values. In this case, the alloy contains some cracks and more micropores inside, which have a greater effect on the hardness of the alloy, and the test will result in more deformation. When the energy density in this study is increased to a certain degree, the cracks and some micropores are eliminated, and the internal tensile stress is in the opposite direction to the loading direction. At this time, the larger the tensile stress, the greater the hardness performance. So in the alloy in the sedimentary state, it is not possible to satisfy both the reduced residual stress to increase the mechanical properties and the increase in alloy hardness to enhance the deformation resistance.

However, once the state of the residual stress is changed, e. g., subjecting the sample to hot isostatic pressing, which causes the cracks to close all the way, reducing the micropores substantially, and applying pressure to release most of the tensile stresses, more deformation will be resisted during testing. The grain state can also be changed through heat treatment, playing the role of grain boundary strengthening, while the grains that are not grown and without other phenomena can also improve the hardness. Therefore, ZGH401 alloy also has a high potential.

5 Outlooks

Additively manufactured superalloys are at the forefront of modern materials research. However, there are a large number of bottlenecks constraining the industrial application of additively manufactured superalloys, especially the crack sensitivity of superalloys. In response to these problems, the Institute of Metals, Chinese Academy of Sciences has developed a nickel-based superalloy ZGH401 for AM, whose cracking can be effectively controlled. In the future, further research should be focused on the microstructural evolution and mechanical property optimization of ZGH401 through hot isostatic pressing, solid solution treatment, and aging treatment. If successful, ZGH401 may become an excellent AM-specific nickel-based superalloy, which in turn can provide theoretical and experimental guidance for designing the next generation of AM superalloys.

6 Conclusions

1) ZGH401 alloy is prepared by SLM at different energy density (33.3−66.6 J/mm^3). With the increase in laser power, the powder in the molten pool is fully melted, which makes the density increase. An excessively high scanning rate reduces laser-matter interaction time, leading to incomplete powder fusion and increased porosity. As the energy density increases from 33.33 J/mm^3 to 66.67 J/mm^3, the porosity decreases from more than 5% to less than 0.1%, and the density increases from 7.91 g/cm^3 to 8.21 g/cm^3.

2) At a constant scanning rate, hardness exhibits a positive correlation with laser power. At minimal laser power and maximal scanning speed, residual stress reaches 411.5 MPa, whereas at maximal laser power and minimal scanning speed, the average residual stress decreases to 359.5 MPa.

3) The SLM-fabricated ZGH401 alloy exhibits a fish-scale-like morphology in its longitudinal section. These fish-scale-like features are formed during molten pool solidification. The overlap between scanning lines within the same deposition layer is optimal, exhibiting no porosity.

4) The precipitates are identified as *M*C carbides that form subgrain together with grains in the build direction and Laves phases. The density of precipitates at molten pool boundaries is less than that within the molten pool interior.

5) Primarily due to the number of grain boundaries, the tensile properties parallel to the build direction are inferior than that perpendicular to it, with average value of 1122.5 and 1147.6 MPa, respectively. The maximum and minimum gaps are 41 and 11 MPa, respectively, and the average value of gaps is 25.10 MPa.

References

1 Bang G B, Park J H, Kim W R *et al*. *Materials Science and Engineering A*[J], 2022, 841: 143020

2 Zhang M, Ma C C, Xue C *et al*. *Rare Metal Materials and Engineering*[J], 2024, 53(8): 2131

3 Wu Shan, Zhou Yang, Shi Zhiwu *et al*. *Materials China*[J], 2024, 43(9): 859 (in Chinese)

4 Wang C Z, Hu Y L, Zhong C *et al*. *Materials Science and Engineering A*[J], 2022, 846: 143276

5 Shahwaz M, Nath P, Sen I. *Journal of Alloys and Compounds*[J], 2022, 907: 164530

6 Wang Yan, Liu Yumeng, Liu Shifeng *et al*. *Materials China*[J], 2024, 43(11): 1035 (in Chinese)

7 Periane S, Duchosal A, Vaudreuil S *et al*. *Materials Today: Proceedings*[J], 2021, 46: 7860

8 Li M H, Wang L L, Yang H O *et al*. *Materials Science and Engineering A*[J], 2022, 854: 143813

9 Ren D Q, Xue Z Y, Jiang Y *et al*. *Engineering Fracture Mechanics*[J], 2020, 239: 107305

10 Chen L, Gu P F, Ge T *et al*. *Materials Science and Engineering A*[J], 2022, 835: 142610

11 Chen F, Wang Q, Zhang C *et al*. *Journal of Alloys and*

Compounds[J], 2022, 917: 165572
12 Huang W Y, Li Y T, Ren Y J *et al*. *Vacuum*[J], 2022, 206: 111447
13 Karabulut Y, Tascioglu E, Kaynak Y. *Optik*[J], 2021, 227: 163907
14 Pu Y N, Zhao D W, Liu B B *et al*. *Rare Metal Materials and Engineering*[J], 2024, 53(8): 2123
15 Dong X, Zhou Y N, Qu Y T *et al*. *Materials Characterization*[J], 2022, 185: 111716
16 Hu T Y, Li W, Yuan S H *et al*. *Materials Today Communications*[J], 2022, 33: 104356
17 Hu Y B, Dong C F, Kong D C *et al*. *Materials Today Communications*[J], 2021, 29: 102994
18 Karimi J, Kollo L, Rahmani R *et al*. *Journal of Manufacturing Processes*[J], 2022, 84: 55
19 Park J M, Kim E S, Kwon H *et al*. *Additive Manufacturing*[J], 2021, 47: 102283
20 Tan Q B, Zhu G L, Zhou W Z *et al*. *Journal of Alloys and Compounds*[J], 2022, 913: 165196
21 Lee J U, Kim Y K, Seo S M *et al*. *Materials Science and Engineering A*[J], 2022, 841: 143083
22 Li B X, Du J, Sun Y J *et al*. *Optics & Laser Technology*[J], 2023, 158: 108806
23 Wu B, Liang J J, Yang Y H *et al*. *China Foundry*[J], 2021, 18: 397
24 Wu B, Liang J J, Zhou Y Z *et al*. *Transactions of Nonferrous Metals Society of China*[J], 2023, 33(4): 1124
25 Ko K H, Kang H G, Huh Y H *et al*. *Journal of the Mechanical Behavior of Biomedical Materials*[J], 2022, 126: 105051
26 Lan L, Wang W X, Cui Z Q *et al*. *Materials Letters*[J], 2023, 330: 133321
27 Ding R G, Zheng J P, Zhang Y Z *et al*. *Materials Science and Engineering A*[J], 2022, 848: 143427
28 Huang Y Y, Xie Z H, Li W S *et al*. *Journal of Alloys and Compounds*[J], 2022, 927: 167011

低能量密度对选区激光熔化制备新型镍基高温合金的组织和性能的影响

徐　鹤[1,2]，梁静静[1,2]，李金国[1,2]
(1. 中国科学技术大学 材料科学与工程学院，辽宁 沈阳 110016)
(2. 中国科学院金属研究所 师昌绪先进材料创新中心，辽宁 沈阳 110016)

摘　要：为了探讨不同能量密度对选区激光熔化（SLM）ZGH401合金的显微组织和力学性能的影响，采用正交试验方法，在不同激光功率和扫描速度下制备了ZGH401合金。采用扫描电镜、电子背散射衍射和电子探针显微分析技术对沉积态ZGH401的微观结构进行了分析。结果表明：随着能量密度的不断增大，沉积态ZGH401的缺陷逐渐减少，相对密度逐渐增大，最终密度可达99.6%。随着激光功率的增加，ZGH401的硬度也随之增加；更快的扫描速度降低了沉积态ZGH401的残余应力。此外，由于垂直沉积方向相比于平行沉积方向晶界更多，因此垂直沉积方向试样的室温拉伸性能更为优异。该合金析出相主要为碳化物和Laves相，熔池边界处的碳化物少于熔池内的碳化物。

关键词：选区激光熔化；低能量密度；ZGH401

作者简介：徐　鹤，男，1997年生，博士生，中国科学院金属研究所师昌绪先进材料创新中心，辽宁 沈阳 110016，E-mail：xuhe1997@126.com